Journal of Materials Chemistry C

Tuning Optoelectronic Characteristics of Ionic Organic Crystalline Assemblies

Journal:	*Journal of Materials Chemistry C*
Manuscript ID	TC-ART-01-2018-000416.R1
Article Type:	Paper
Date Submitted by the Author:	14-Feb-2018

Complete List of Authors:	Borders, Bryan; Washington State University, Chemistry Adinehnia, Morteza; Washington State University, Chemistry Chilukuri, Bhaskar; Washington State University, Chemistry Ruf, Michael; Bruker AXS Inc., SC-XRD Product Hipps, K W; Washingotn State University, Chemistry Mazur, Ursula; Washington State University, Chemistry

Journal Name

ARTICLE

Tuning Optoelectronic Characteristics of Ionic Organic Crystalline Assemblies

Received 00th January 20xx,
Accepted 00th January 20xx

DOI: 10.1039/x0xx00000x

www.rsc.org/

Bryan Borders,[a] Morteza Adinehnia,[a] Bhaskar Chilukuri,[a] Michael Ruf,[b] K. W. Hipps,[a*] and Ursula Mazur[a*]

The effect of selective metallation of free-base ionic porphyrin tectons on the structural, electronic, and optical properties of their crystalline self-assemblies is presented. Rod-like crystals were prepared under neutral pH conditions by combining *meso*-tetra(N-methyl-pyridyl)porphyrin, H_2TMPyP, and *meso*-tetra(4-sulfonatophenyl)porphyrin, H_2TSPP, with either a nickel or copper ion contained in one of the synthons. These materials were characterized by optical microscopy, X-ray diffraction methods, thermogravimetric analysis, diffuse reflectance UV-visible and luminescence spectroscopies, and conductivity and photoconductivity measurements. All the porphyrin assemblies formed monoclinic $P2_1/C$ crystals with pseudo-hexagonal cross sections. Themogravimentric experiments indicate that water molecules associated with crystals desorb at two different rates. In addition, the temperature dependent XRD showed that the dehydration of the porphyrin solids causes modification in the crystals which is completely reversible up 100 °C annealing (i.e., crystals return to their original structural geometry upon rehydration). All the metallated porphyrin crystals exhibit dark conductivity at moderately high temperatures and become more conducting upon photoexcitation. The photoresponse of the H_2TMPyP:CuTSPP-substituted crystals is significantly higher than that of the CuTMPyP:H_2TSPP and the Ni-substituted crystals. This Cu-substituted system also exhibits persistent photoconductivity resulting from excitations into the Q and Soret bands. The primary charge carriers in these solids upon photoexcitation are electrons and the charge recombination mechanism follows monomolecular kinetics. Quantum mechanical calculations provide the electronic band structure, the density of states and explain the experimental prompt photoconductivity measurements of the porphyrin self-assemblies. This work provides evidence that optoelectronic properties of organic semiconductors can be effectively tuned by introducing transition metals into their crystal structures.

Introduction

Organic semiconductors composed of extended π-conjugated molecular systems exhibit high photoelectrical responsivity because of their large absorption coefficient (c.a. 10^5 L/mole-cm),[1] and are well known for their efficacy in developing novel electronic and photonic devices for light detection, energy conversion and storage, and memory. In comparison with their inorganic counterparts, organic semiconductors have advantages of being lightweight, flexible, and easily fabricated.[2] Their processing can be conducted at lower temperatures than Si-based materials and may be carried out in solution thus reducing the costs of fabrication.[3,4] Another characteristic of organic semiconductors is their directional electrical conductivity, which contrasts the typical three-dimensional electrical transport in inorganic semiconductors. In organic materials, charge carriers travel through overlapping π orbitals and, therefore, controlled molecular organization is important for device performance. For high performance optoelectronic devices, single crystal organic structures are preferred because they tend to be free of large structural defects (e.g., grain boundaries) that can limit charge transport mobilities.[3,5,6] Single crystals are also important tools for conducting fundamental quantitative studies linking structure to charge and energy transport as well as intrinsic optical properties of organic semiconductors.

Ionically self-assembled (ISA) porphyrins are particularly good single crystal candidates for model structure–electronic properties correlation studies. This robust class of π-conjugated chromophores possess panchromatic behaviour with strong absorption across the near-ultraviolet to near-infrared region and are potentially useful as active components of solar cells,[5,7-10] sensors,[11-18] photocatalysts,[19-22] and photovoltaics.[23-26] The molecular organization in ionic porphyrin solids is controlled by strong electrostatic attraction, π-π interactions, and hydrogen bonding. The presence of the strong Coulombic attraction in ionic porphyrin crystals contributes significantly to their structural stability which promotes good charge transport (due to high π-orbital overlap) and favorable optoelectronic

[a] *Department of Chemistry and Materials Science and Engineering Program, Washington state university, Pullman, WA, 99164-4630, USA.*
**E-mail: umazur@wsu.edu Tel: +1-509-335-5822*
[b] *Bruker AXS Inc, Madison, WI, 53711, USA.*

†Electronic ESI† (ESI) available: ESI contains atomic coordinates and isotropic displacement parameters. Luminescence, field effect, and temperature dependent conductivity data are also provided. See DOI: 10.1039/x0xx00000x

properties without compromising their mechanical flexibility.[27-29]

We have recently reported a comprehensive structure-property correlation study of a model single crystal ionic binary π-molecular system using both experimentation and theory.[30] The experimental system was based on ionic photoactive porphyrin synthons, namely *meso*-tetra(N-methyl-4-pyridyl)porphyrin $(H_2TMPyP)^{4+}$ and free-base *meso*-tetra(4-sulfonatophenyl)porphyrin $(H_2TSPP)^{4-}$. We demonstrated that single crystals of H_2TMPyP:H_2TSPP can be grown in a controlled and reproducible manner with the desired composition, size, and dimensionality. Single crystal structure data was used to predict the morphology and to provide better understanding of conductive behavior of the H_2TMPyP:H_2TSPP organic structure. Furthermore, we showed that electronic structure calculations can provide insights into the optical and electronic properties of these materials. In the current work we employ our newly developed predictive growth algorithm and computational procedures to tune the optoelectronic properties of the H_2TMPyP:H_2TSPP crystals by selectively metallating the free-base ionic porphyrin parent tectons. The goal is to optimize electrical and photo response of these ISA binary porphyrin (BP) crystalline semiconductors.

The systems of interest here are nickel(II) and copper(II) substituted H_2TMPyP:H_2TSPP single crystals where a metal ion is present in one or both of the synthons. The presence of metal ions can potentially narrow the bandgap and/or introduce midgap bands to increase charge transport in the resulting binary porphyrin systems and increase their photoresponse. Hence, the motivations for using metalled porphyrin cores are to (1) examine their impact on the crystal structure as it relates to their parent metal free H_2TMPyP:H_2TSPP system, (2) evaluate the physical stability of the metallated porphyrin crystals, (3) measure the breadth of their optical responsivity and (4) access their dark current conductivity and photoconductivity yields. To accomplish these objectives, we employed both experimental and theoretical methods. Single crystal structures of the metallated ISA porphyrins were determined using X-ray diffraction (XRD). The thermal stability and integrity of the crystalline solids were evaluated using thermogravimetric analysis (TGA) combined with powder XRD studies. UV-visible diffuse reflectance spectroscopy (DRS) and luminescence spectroscopy combined with photoconductivity studies were carried out to investigate local electronic structure and to probe the dynamics of photoexcitation. DFT calculations were carried out to explain the experimental photoconductivity measurements. The conduction process is related to the molecular structure, type of metallic core, and organization of the porphyrin tectons within the crystalline assemblies.

Experimental Methods

Materials

Porphyrin compounds purchased from Frontier Scientific included meso-tetra(4-sulfonatophenyl) porphyrin dihydrochloride, $[H_2TSPP]_2HCl$, tetra-sodium meso-tetra(4-sulfonatophenyl) porphyrin, $Na_4[H_2TSPP]$, meso-tetra(N-methyl-4-pyridyl) porphyrin tetrachloride, $[H_2TMPyP]Cl_4$, Cu(II) meso-tetra(4-sulfonatophenyl) porphyrin, $H_4[CuTSPP]$, Ni (II) meso-tetra(4-sulfonatophenyl) porphyrin, $H_4[NiTSPP]$, and Ni (II) meso-tetra(N-methyl-4-pyridyl) porphyrin tetrachloride, $[NiTMPyP]Cl_4$, (all 99% pure). They were used without further purification. Millipore (18.1 MΩ) water was employed exclusively. Acetonitrile (J.T. Baker), methanol (Decon Labs), and KBr (J.T. Baker) were all reagent grade. Porphyrin stock solutions (1000 μM in 4:1 H_2O:ACN) were used within two weeks' time of initial preparation. All solution pH adjustments were made with trace-metal grade HCl (Fisher Scientific) and NaOH (J.T. Baker) at 2 mM and 1 M, respectively.

Synthesis of BP crystals

All porphyrin ISA synthesis were carried out in a batch reactor in a temperature controlled Brinkmann bath as previously described.[31] Solution of individual porphyrins were preheated to 333 K prior to mixing. Reactions were allowed to proceed for approximately 20 hours. The following ISA reactions were carried out:

$$H_2TMPyP^{4+}{}_{(aq)} + H_2TSPP^{4-}{}_{(aq)} \rightarrow H_2TMPyP{:}\,H_2TSPP_{(s)}$$
$$CuTMPyP^{4+}{}_{(aq)} + H_2TSPP^{4-}{}_{(aq)} \rightarrow CuTMPyP{:}\,H_2TSPP_{(s)}$$
$$H_2TMPyP^{4+}{}_{(aq)} + CuTSPP^{4-}{}_{(aq)} \rightarrow H_2TMPyP{:}\,CuTSPP_{(s)}$$
$$H_2TMPyP^{4+}{}_{(aq)} + NiTSPP^{4-}{}_{(aq)} \rightarrow H_2TMPyP{:}\,NiTSPP_{(s)}$$
$$NiTMPyP^{4+}{}_{(aq)} + H_2TSPP^{4-}{}_{(aq)} \rightarrow NiTMPyP{:}\,H_2TSPP_{(s)}$$

After the porphyrins ISAs crystallized, small aliquots of a suspension were withdrawn for crystallographic, spectroscopic, conductivity and microscopic analysis.

Optical microscopy

A drop of porphyrin crystal suspension was placed on a glass microscope slide and a cover glass was placed on top of the drop to spread the liquid and immobilize the motion of the crystals. Optical images of the crystals were obtained with and without polarization using a Leitz Aristoplan Microscope.

X-Ray diffraction

For single crystal XRD evaluation, suitable H_2TMPyP:NiTSPP needle-like crystals were selected and cut to smaller dimensions. A Bruker D8 VENTURE single crystal diffractometer equipped with a Ga METALJET X-ray source (1.341398 Å) and Photon 100 detector was used for data collection. The details of data collection and structural refinement are summarized in Table S2 (ESI†). The atomic coordinates, isotropic and anisotropic parameters, and selected bond distances and angles are given in Tables S3-S6 (ESI†). Also, a crystallographic information file (cif file) is available in the ESI.†

Powder X-ray diffraction measurements were conducted to evaluate the crystallinity of the porphyrin solids as a function of temperature. The samples were mounted in a SmartLab (Rigaku) diffractometer (Cu Kα radiation- D/tex ultra linear position sensitive detector) in parallel beam configuration, equipped with an Anton Paar XRK 900 heater chamber and under Argon as carrier gas (15 ml/min). Samples were heated at

2 °C/ min until the analysis temperature was achieved and then stabilized for 3 min before the scan. Diffraction patterns were obtained in the range of 4–30 2θ degrees at a scan rate of 1.5 °/min.

Thermogravimetric analysis (TGA)

TA Instruments TGA Q50 was used for the thermogravimetric studies of the porphyrin crystals. Temperature precision was ±1 °C and weighting precision and sensitivity were ±0.01 % and 0.1 µg, respectively. All experiments were performed under the flow of nitrogen gas (60 ml/min) and the heating rate of 2 °C/min. Typically, a sample of solid porphyrin was placed in the platinum pan and heated from room temperature to 300 °C.

UV-visible diffuse reflectance spectroscopy (DRS)

The porphyrin crystals were isolated by filtering their solid suspensions through 100 nm pore size, 47 mm Teflon filter membranes (Membrane Solutions) using a Millipore vacuum filtration setup, after which the solids were dried. DRS samples were prepared by grinding small amounts of each ISA solid in a small amount of KBr such that the final concentration of the porphyrin was about 0.2 wt% in each of the samples. The powders were loosely pressed in a metal anvil cell outfitted with a 1 cm quartz window. Reflectance spectra were collected using a ThermoFisher Bio 260 UV-vis Spectrophotometer equipped with an ISA-220 integrating sphere. All reflectance data was processed using the Kubelka-Munk transform.

Luminescence spectroscopy

Laser-induced steady state emission spectra were collected with a home-built luminescence spectrometer outfitted with a 408 nm cw-diode laser (Coherent Model 0222-583-00, ~2 mW). Details of the experimental setup can be found elsewhere.[32] The width (O.D.) of the sample tube was 2 mm and the beam diameter at the sample was 25 µm. Luminescence spectra of the monomers, 1:1 molar ratio physical mixtures of the monomers, and those of the ISA solids were measured. No change in the luminescence intensity was observed for any of the samples during data collecting, indicating that no sample photodecomposition took place. All spectra were corrected against an Ocean Optics calibrated light source (model HL3-INT-CAL, spectral irradiance standard).

IDE preparation and treatment

Gold interdigitated electrodes (IDEs) (from UC Santa Barbara Nanofabrication Facility) with a spacing of 10 µm were used for the conductivity and photoconductivity experiments. Two variations of the IDEs were used; Au electrodes fabricated directly on glass or on top of a 400 nm thick SiO_2 layer supported on a p^{++} doped silicon chip. The glass supported IDEs were employed in the measuring the conductivity and the photoconductivity of the porphyrin rods while the IDEs deposited on silicon chips were employed in field effect experiments of the crystalline composites. Typically, the ISA crystals were deposited on the IDEs by placing a drop of liquid porphyrin crystals suspension atop the IDE, allowing the solution to sit for an hour, and then wicking away any excess solution with a Kimwipe tissue. The IDE was then examined under an optical microscope to determine if a sufficient number of porphyrin crystals were present on the IDE. This process was repeated until approximately 50% of the surface was covered with BP rods.

The IDEs on glass provided the option for sample illumination from either side of the glass substrate. Both illumination directions yielded comparable conductivity and photoconductivity profiles for the ISA crystals, however higher current signals were obtained with the laser directed from the bottom of the glass slide (the side in contact with the Au IDE). This latter illumination format was adopted for all the conductivity and photoconductivity experiments unless otherwise indicated.

Conductivity and photoconductivity measurements

All conductivity and photoconductivity measurements were made at +5 V bias, unless otherwise indicated. Note that in the sample configuration described previously, we measured parallel conductivity ($\sigma_{||}$) where charge flow proceeded along the columns of stacked porphyrins. Measurements of perpendicular current in nearly one-dimensional nano to microcrystals such as the BPs are difficult. Conductive AFM[33] is the appropriate tool for such experiments, which will be carried out at a later date and comprise a publication of their own.

Action spectra, time dependence, temperature dependence, and field effect experiments were measured in an in-house designed vacuum chamber with a base pressure <5 mTorr.[30] Prior to all measurements, the porphyrin samples were heated to 373 K under vacuum for at least 12 hours. Source-drain biases (V_{SD}) was applied using a Data Translation DT9836 data acquisition system (DAQ). The current was measured using a Keithley 427 current amplifier and recorded by the DT9836

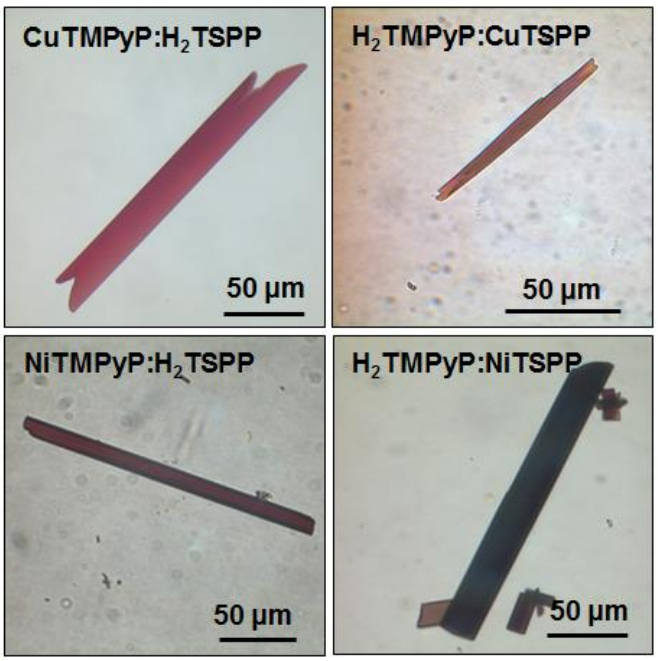

Fig. 1 Optical images metallated ISA porphyrin crystals.

DAQ. A Keithley 246 high voltage supply was used to apply gate voltages (V_G). Variable power 406, 445, 473, 532, and 671 nm diode lasers and a 632.8 nm HeNe laser were used as excitation sources. These wavelengths were selected based on the measured absorbance spectra of the BPs. The laser beams were focused to a 1 mm diameter spot size. A calibrated photodiode was used to monitor the laser power during all experiments. Illumination experiments were performed using a Measure Foundry (Data Translation, Inc.) program designed to control and record V_{SD} and record the time, current, and photodiode signal.

Current-time (I-t) curves were collected by applying V_{SD} = 5 V and V_G = 0 V while recording the current. A baseline was measured for 1000 s in the dark, and then the sample was illuminated with 406, 445, or 671 nm irradiation until saturation current was reached. Illumination was then terminated, but measurement of the current continued for at least 30 minutes. These experiments were performed at 298, 323, 348, and 373 K.

Periodic modelling

Calculations on all the ISA crystals were performed using the Vienna *Ab initio* Simulation Package (VASP)[34,35] version 5.2 and with extended Hückel tight binding (EHTB)[36-40] method. VASP calculations were done using the Perdew-Burke-Ernzerhof (PBE)[41] exchange-correlation functional with plane-wave basis set and projector augmented wave (PAW)[42,43] potentials. A plane-wave (PW) energy cut-off of 450 eV was applied. The H_2TMPyP:NiTSPP crystal structure obtained from single crystal-XRD was used to model all metallated BPs. The calculated BP models include H_2TMPyP:NiTSPP, NiTMPyP:H_2TSPP, H_2TMPyP:CuTSPP and CuTMPyP:H_2TSPP. The water molecules in the crystal structure were removed in the periodic calculations to determine the electronic properties of only the BPs. All structures were optimized with a gamma point until the energy convergence of 0.0001 eV. Each optimized structure was used to perform self-consistent field (SCF) calculations with a *k*-point grid of 9 x 6 x 4 in the irreducible Brillouin zone (BZ) of the monoclinic cell using the Monkhnorst and Pack (MP) method.[44] All DFT calculations were performed with dispersion corrected vdW-DF functional[45,46] of Klimes, Langreth, and Lundqvist *et al*. which takes into account the non-local nature of electron correlation. This functional is the optB88-vdW GGA[47] with PBE potentials. It was previously reported[48] that calculations with dispersion corrected vdW-DF functional yields better geometries and properties when compared with experiment than with conventional DFT functionals.

Additional calculations on the aforementioned complexes were performed with extended Hückel tight binding (EHTB) method. It is well documented that DFT underestimates the band gap in a variety of systems[49-51] and that EHTB is an inexpensive yet reliable alternative for band structure calculations.[52-54] We used the VASP optimized metal-BP structures to perform EHTB calculations. The EHTB calculations using the virtual nano lab-atomistic toolkit (VNL-ATK) software package.[56] Upon evaluation of Hoffmann and Muller parameters (basis sets) within the ATK-VNL package on metal-BP systems, we have determined that Hoffmann parameters work better for main group elements while Muller parameters work better for complexes containing transition metals and main group elements. We validated the results by comparison to DFT calculations and experimental data. As the present systems contain transition metals (Ni, Cu), all our EHTB calculations were performed with Muller parameters. The off-diagonal elements of the Hamiltonian are evaluated with the Wolfsberg-Helmholtz formula. Numerical integrations over the symmetry-unique section of the Brillouin zone of the crystal structure of the BPs were performed using a set of 76 *k*-points. Calculated matrix data was then used to plot the band structure. Using the band structure, the effective masses of electrons and holes at Gamma point (Γ) were calculated.

Results and Discussion

Synthesis and crystal Structure

The ISA porphyrin crystals synthesized include NiTMPyP:H_2TSPP, H_2TMPyP:NiTSPP, CuTMPyP:H_2TSPP, and H_2TMPyP:CuTSPP. They were fabricated from +4 and -4 charged porphyrin synthons under reproducible and controlled conditions described earlier.[30,31] The notation used in identifying the different tecton pairs is for brevity and reflects the numbers of protons associated with the core nitrogens. All four metallated ISA composites were grown in 4:1 H_2O:acetonitrile (neutral pH) 20 μM at 65 °C solutions forming rod-like crystals and are shown in Figure 1.[30] The ionic tecton stoichiometric ratio was 1:1 for all the metal substituted porphyrin ISA systems fabricated. This ratio was verified by XPS measurements and the results are provided in figures S1 through S4 and Table S1).

A comparison of the powder XRD patterns of the metallated porphyrin materials with the diffraction pattern obtained from

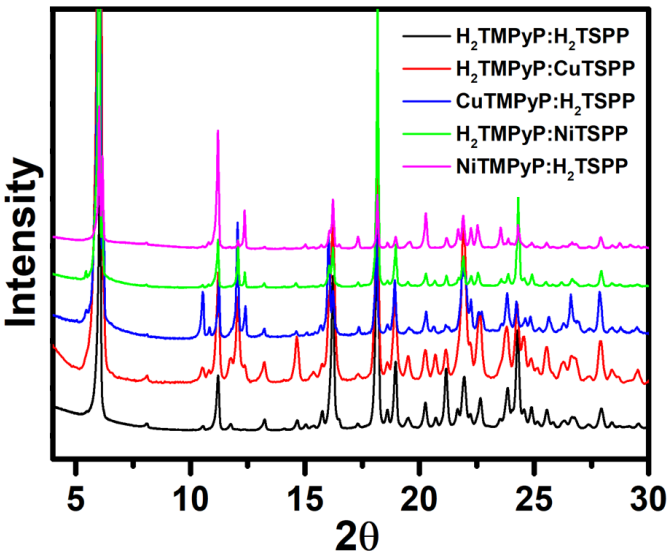

Fig. 2 Comparison of the powder XRD patterns of the free-base and metallated ISA porphyrin crystals. The baselines of the XRD patterns are offset for easier comparison.

the free-base system is depicted in Fig. 2. Peak positions

observed in the XRD patterns of the metal substituted composites match the positions in the pattern obtained from the metal-free H_2TMPyP:H_2TSPP crystals however, the intensities of the observed peaks vary among the patterns. Because the diffraction peak positions are nearly identical for all four compounds this indicates that the substitution of one of the free-base porphyrins with the Ni(II) or Cu(II) ions does not modify the crystal structure of the final ion pair product. Variations in peak intensities can be observed in the indexed (002), (021), (110) and (202) reflections (Fig. S5 in ESI†). These planes intersect the metal atoms (copper or nickel) present in the unit cell of the porphyrin crystal. Since transition metals in general have a higher atomic scattering factor than elements like carbon or nitrogen, more intense diffraction peaks are measured for reflections containing heavy elements (see Fig. S5 in ESI†).[57] We note that XRD powder patterns of ISA crystals with metals in both ionic tecton cores, for example NiTMPyP:NiTSPP, were different than those in Fig. 2 (see Fig. S6 in ESI†). Thus, binary substitution does change the structure.

Single crystal data was obtained from a high quality H_2TMPyP:NiTSPP crystal. The resulting structure is shown in Figure 3. The space group for the complex was determined to be a monoclinic $P2_{1/c}$ with unit cell dimensions of a = 8.3287(5) Å, b = 16.3760(10) Å, c = 29.1881(19) Å, β = 92.363(3)° and volume = 3977.6(4) Å^3. Reliability factor, R, equalled to 5.42% indicating an excellent agreement between the experimental X-ray diffraction data and the crystallographic model. The unit cell parameters of the H_2TMPyP:NiTSPP crystals are nearly identical to those previously reported for the H_2TMPyP:H_2TSPP crystals (a = 8.3049(11) Å, b = 16.413(2) Å, c = 29.185(3) Å, β = 92.477(9)° and volume = 3974.4(8) Å^3), a further corroboration that the metal-free and metallated crystals retain nearly identical crystal structures.[30]

Fig. 3a depicts a cross-section of the *cb* crystallographic plane, in which molecules are composed of half each, the $[H_2TMPyP]^{4+}$ and the $[NiTSPP]^{4-}$ ions. The molecular slabs in this direction are not flat. In the structure two of the sulfonate groups in the $[NiTSPP]^{4-}$ units bear six oxygens instead of the expected three as a result of disorder.[58] The percent occupancy of oxygens is consistent with three atoms per each sulfonate functionality.

Along the crystal growth direction, the *a* axis, the porphyrin macrocycles form coherent columns (Fig. 3b and Fig. S7 in ESI†) of alternating ions with their planar centers slightly offset relative to each other. The phenyl sulfonyl substituents on the porphyrin rings are rotated relative to the macrocyclic planes by 50.7° and adopt vertically parallel alignment within the macrocyclic columns (Figure 4b). The interplanar separation of the porphyrins is 0.384 nm while the centroid distance is 0.416 nm, which is identical to free base only ion pairs.[30] As in the case of H_2TMPyP:H_2TSPP crystals, there are five water molecules per porphyrin dimer located in the channels between the porphyrin columns of the H_2TMPyP:NiTSPP crystals (only the oxygens are shown in Fig. 3).

TGA and temperature dependent XRD

The impact of heating on the integrity of crystal structures of the compounds was examined by performing concomitant TGA and powder XRD studies of the ISA solids. Thermal stability of crystalline organic molecular semiconductors is an important processing parameter as it may affect their optoelectronic properties. Figure 4 shows representative TGA profiles for both the H_2TMPyP:H_2TSPP and the H_2TMPyP:NiTSPP crystals. Similar plots were obtained for the NiTMPyP:H_2TSPP, the CuTMPyP:H_2TSPP and H_2TMPyP:CuTSPP composites (see Supporting Information). The TGA profiles of both the H_2TMPyP:H_2TSPP and the H_2TMPyP:NiTSPP solids are nearly identical. They indicate significant changes in the mass of the porphyrin crystals for three discrete temperature regions: 295-

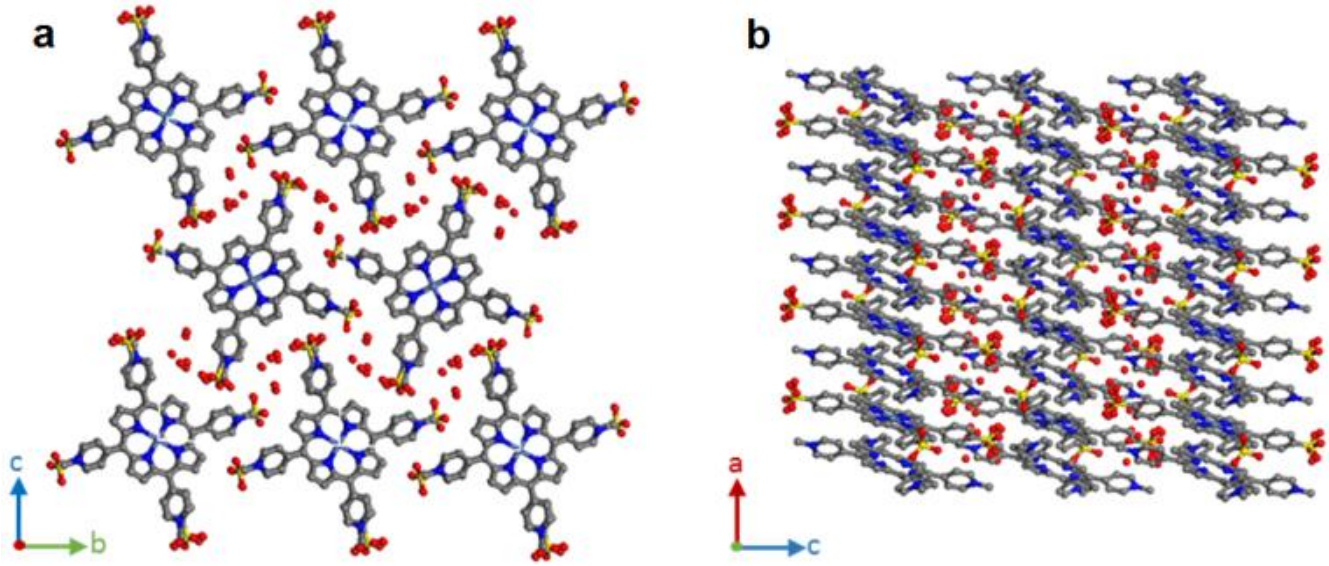

Fig. 3 Crystal structure of the H_2TMPyP:NiTSPP nanorods in two different orientations; (a) direction normal to the crystallographic *a* axis and placements of water molecules (isolated red oxygen atoms) in the intermolecular space; (b) direction normal to the crystallographic *b* axis, showing alternating $[H_2TMPyP]^{4+}$ and $[NiTSPP]^{4-}$ porphyrin tectons within the columns. Color codes: blue, N; grey, C, yellow; S; red, O (hydrogens not shown).

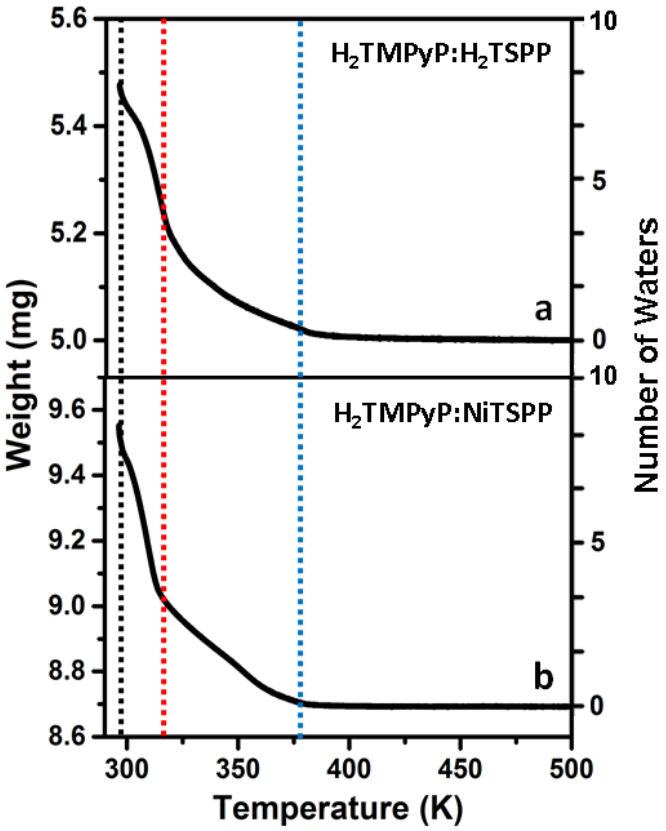

Fig. 4 Comparison of the TGA curves obtained for the (a) H_2TMPyP:H_2TSPP and (b) H_2TMPyP:NiTSPP crystals. The broken black, red, and blue lines specify, respectively, temperature regions in which the surface water molecules and the waters residing in the crystal channels are removed.

320 K, 320-380 K, and above 380 K. The reduction in mass that results in heating to 320 K corresponds to a calculated loss of approximately 4.5 water molecules per porphyrin dimer while the second heating segment is consistent with the removal of additional three waters for each ion pair. At temperatures above 380 K the slope of the TGA plot no longer changes indicating no further reduction in the mass of the sample. (The decomposition temperature for the metallated and free-base BPs is in the range of 380 K to 382 K.) Since the diffraction data

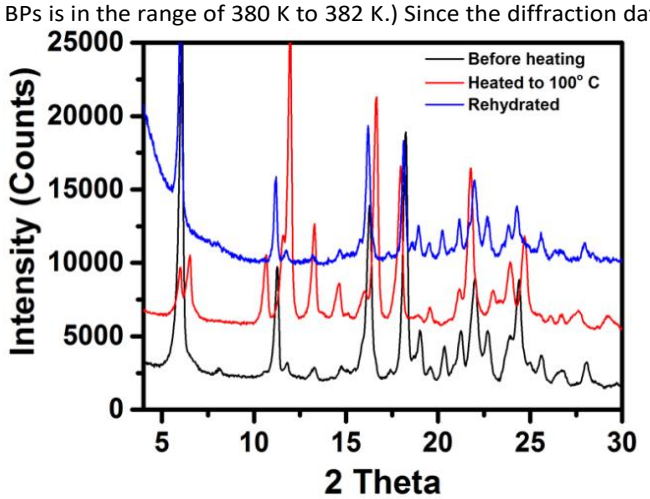

Fig. 5 Comparison of the powder XRD patterns obtained from a H_2TMPyP:H_2TSPP sample before heating (black), after heating to 100° C (red) and after rehydration of the crystals (blue).

refinement for both the H_2TMPyP:H_2TSPP and the H_2TMPyP:NiTSPP crystals specifies the presence of 5 water molecules per ion pair, it is likely that the sample weight loss recorded (295-380 K range) corresponds to water desorption from the surface of the rods as well as from the internal cavities of the rods. This accounts for the loss of 7.5 water molecules in total .The initial water molecules leaving the ISA solid include surface water (2.5 per ion pair) and weakly bound water present in crystal cavities (2 per tecton pair). The remaining H_2O (3 per ion pair), which is more strongly bound requires higher annealing temperatures to remove.

Figure 5 depicts the powder XRD patterns of H_2TMPyP:H_2TSPP crystals collected at 25 °C (prior to heating), after heating to 373 K, and after exposing the heated sample (cooled to room temperature) to water vapour. Heating the crystals to 100 °C (red trace in Figure 5) clearly causes significant changes in the diffraction pattern of H_2TMPyP:H_2TSPP when compared to the same sample at room temperature (black trace in Figure 5). This change is likely due to the loss of the water molecules from within the crystalline channels. Interestingly, the heated sample when rehydrated, exhibits the same XRD pattern as the diffraction data acquired from an original unheated sample. Analogous results were obtained for the dehydration/rehydration XRD studies of a H_2TMPyP:NiTSPP sample heated to elevated temperatures (see Fig. S8 in ESI†). Based on the similarities of their crystal structures and parallel TGA profiles it is reasonable to assume that the dehydration/rehydration characteristics of H_2TMPyP:H_2TSPP and H_2TMPyP:NiTSPP are shared by the other metallated analogues for annealing temperatures near 100 °C. We note that heating the ISA porphyrin crystals above that temperature may irreversibly change their structure. This was observed in the case of H_2TMPyP:NiTSPP (see Fig. S9 in ESI†) and the tetrapyridylporphyrin:TSPP (TPyP:TSPP) system.[59] When the H_2TMPyP:NiTSPP and TPyP:TSPP crystals were heated above 100 °C they transitioned from crystalline to a partially amorphous structure.

It is gratifying to observe the high thermal stability of the ISA porphyrin assemblies. The strong electrostatic interactions preserve the integrity of the crystal structures even when annealed and minimize the potential impairment of their conductive and photoconductive properties (as demonstrated below). ***The dehydration/rehydration process is completely reversible suggesting the potential* usage *of the H_2TMPyP:H_2TSPP crystals (and the metallated versions) as gas sensors.*** Our laboratory is currently testing such applications.

Absorbance and luminescence spectra

Fig. 6 depicts the UV-vis DRS spectra of the ISA crystals overlaid with the summed spectra collected from the parent synthons. The Soret bands of all the ISA systems appear near 420 nm and have similar intensities. The Q-bands however, exhibit considerably different intensities for the different porphyrin ion combinations. The two Ni (II) substituted ISA crystals, in particular, show significantly stronger absorbance in this region than either the metal-free or the Cu-substituted

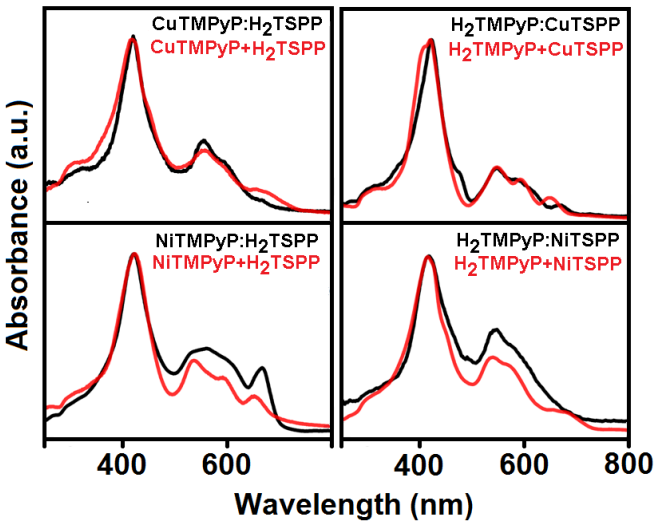

Fig. 6 Overlaid electronic DR spectra obtained from the ISA crystals (black) and the co-added spectra from the parent monomers (red). All the spectra are scaled to the Soret band.

system (for additional spectra, see Fig. S10 in the ESI†). While the spectrum of the H_2TMPyP:H_2TSPP crystals is nearly identical to the sum of the spectra of its parent synthons, the spectra of the metallated crystals show significant changes within the Q-band region when compared to the sum of the spectra of their constituent synthons. These spectral changes suggest an increase in the electronic communication between the porphyrin molecules in the metallated crystals when compared with the metal-free crystal system.

While the metal-free ISA crystals exhibited a strong red-shifted broad emission band[30] the metal-substituted ISAs show almost no luminescence compared to the spectrum of the equimolar mixture of the parent synthons (Fig. S10 in ESI†). The intensity from the photoluminescence of the mechanically mixed porphyrins at 734 nm is dominated by the Q band emission from TMPyP. The solid state luminescence of TMPyP is similar to its emission spectrum in solution under neutral pH conditions.[60] The TSPP free-base emission band from a powder sample is extremely weak unlike the fluorescence from the TSPP diacid in solution which is much more intense.[61,62] The NiTMPyP and NiTSPP solid state monomers are also weak emitters while CuTSPP shows moderately strong luminescence (Fig. S10 in ESI†). Cu(II) porphyrins are known to luminesce[63] whereas Ni(II) complexes do not. For example, Harriman observed that Ni(II) *meso*-tetraphenylporphyrin (NiTPP) was non-luminescent, while free-base TPP, ZnTPP, and MnTPP all exhibited luminescent behaviour.[64] The lack of luminescence in NiTPP was attributed the rapid internal conversion from the lowest excited state of the porphyrin to a d-d transition band on the Ni. Theoretical calculations[65] and triplet quenching experiments[66] estimated this d-d state lies approximately 8000 cm^{-1} (0.99 eV) above the ground state. Several other groups have observed similar transient absorption behaviour from Ni(II) porphyrins.[67-70] It is therefore likely that a similar mechanism is responsible for the quenching of the luminescence in the H_2TMPyP:NiTSPP and the NiTMPyP:H_2TSPP ion-paired chromophores in the solid state.

Earlier we reported that the broad H_2TMPyP:H_2TSPP emission centered at 807 nm might be due to a low-lying CT transition.[30] Similarly the very weak red-shifted (875 nm) luminescence of the H_2TMPyP:CuTSPP crystalline solid relative to the emission from its monomers suggests that there are lower energy excited states that are unique to the ISA porphyrin system. Recently, Natale and Scandola attributed strong emission quenching from ion pairs of free base and zinc substituted TMPyP and TSPP in dilute fluid solutions to the formation of a non-luminescent charge-transfer state below the lowest excited states of the porphyrin molecules.[71] From the electrochemical data they provide, the energy of the H_2TMPyP:H_2TSPP dimer can be estimated as 1.47 eV above the ground state. The observed luminescence for H_2TMPyP:H_2TSPP and H_2TMPyP:CuTSPP (Fig. S10 in the ESI†) have maxima at 1.49 eV and 1.42 eV, respectively, suggesting that their origin may indeed be a charge delocalized state.[71] The CuTMPyP:H_2TSPP system did not luminesce.

Photoconductivity and dark conductivity

All four metallated ISA systems are photoconductive (Fig. S11 in the ESI†). Fig. 7 shows the comparisons of the UV-vis DRS spectra with the photoconductivity action spectra of the BP materials. As in the case of the H_2TMPyP:H_2TSPP,[30] the action spectra and UV-vis spectra of the H_2TMPyP:CuTSPP, CuTMPyP:H_2TSPP and H_2TMPyP:NiTSPP crystals mirror each other. These close similarities along with the linear dependence of the photoconductivity on the power of the excitation source (Fig. S12 in ESI†) suggest that the number of electrons contributing to the photocurrent is directly proportional to the number of photons absorbed. These data also suggest that the mechanisms of the photoconductivity resulting from excitations within the Soret band and the Q-band are the same.

Interestingly, the absorption spectrum and action spectrum of the NiTMPyP:H_2TSPP crystals (Fig. 7) are significantly

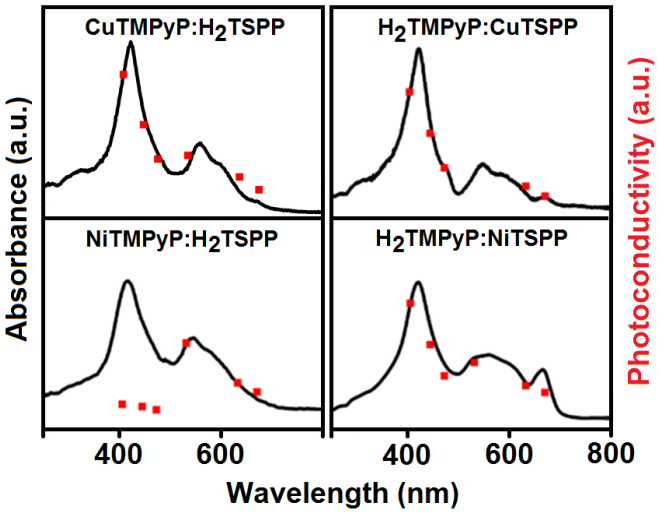

Fig. 7 Absorbance (black trace) and action spectra (red points) of different ISA porphyrin crystalline assemblies.

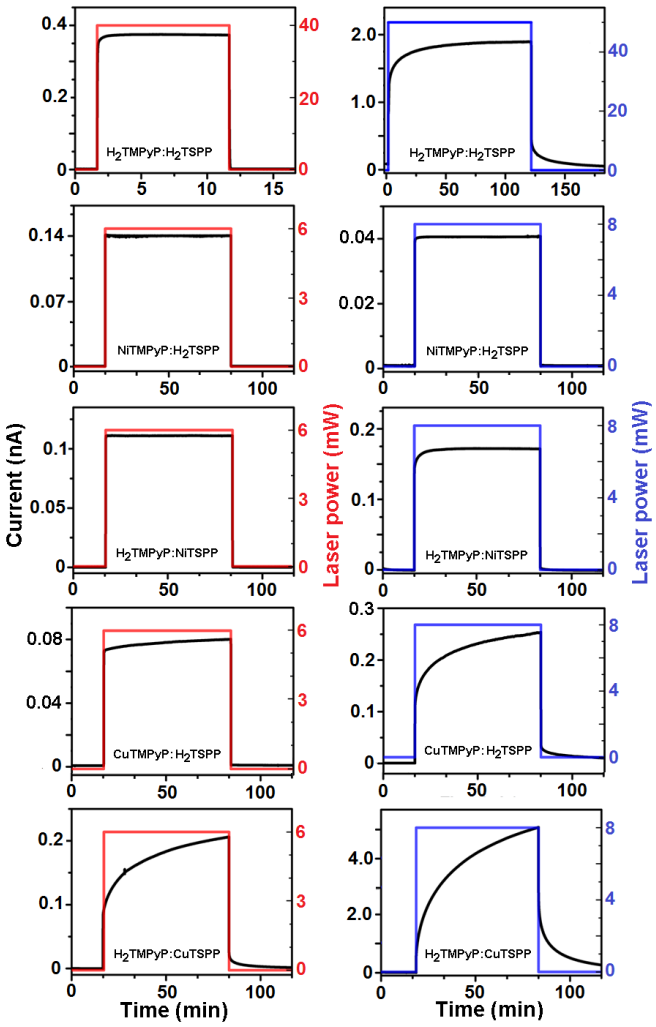

Fig. 8 Comparison of time-dependent photoconductivity of metalled and free-base ISA porphyrin crystals collected at room temperature. Data in the left column was obtained with 671 nm illumination graphs on the right was acquired with 445 nm laser source.

different from one another, yielding much more photoconductivity with excitation in the Q-band region than with excitation in the Soret region. This suggests that the photoconductivity resulting from excitation in the Soret band is severely quenched. The photoconductivity of the NiTMPyP:H_2TSPP crystals is linearly dependent on power for both the Q and the Soret band excitations (see Fig. S11 in the ESI†).

The primary charge carriers of all four metal-substituted crystals (as well as for the H_2TMPyP:H_2TSPP system[30]) were determined to be electrons based on the results of field-effect experiments (Fig. S13 in the ESI†). In these trials, V_{SD} was held constant while the gate voltage, V_G, was varied. The measured current was then plotted with respect to the applied gate voltage.[72,73] Based on these results, these binary porphyrin series are n-type photoconductors.

The recombination mechanism of the photogenerated charge carriers in the free-base and metal substituted porphyrin crystals was estimated from plots of photocurrent (I) variation with laser power (P) plots for these systems (Fig. S12 in the ESI†). A power law dependence relationship of $I \propto P^{\alpha}$ yielded a value of $\alpha \approx 1$ which is consistent with unimolecular (geminate) recombination mechanism. Values of 0.5 and 1.0 specify a bimolecular and unimolecular charge recombination mechanisms, respectively.[74-76] Bimolecular process consists of two free carriers combining simultaneously such as direct band-to-band electron-hole recombination. Unimolecular kinetics involves the recombination of one free carrier at a time (e.g., an electron captured by a recombination center and then recombined with a hole; carrier loss to electrodes or to a trap) primarily originating from trapping of charges.[74-76]

Representative time dependent photoresponsivity of free-base and the metallated porphyrin crystals subjected to 445 nm and 671 nm excitation wavelengths at 25 °C are depicted Fig. 8 (see also Fig. S14 in the ESI†). The photoconductivity (PC) graphs for the H_2TMPyP:NiTSPP and NiTMPyP:H_2TSPP exhibit a sharp rises in photocurrent with the onset of illumination, followed by a flattening of the response curve. When the illumination is terminated, a sharp drop in the signal is observed. The PC response was prompt and reproducible with on/off illumination both at 445 nm and at 671 nm. The I-t curves obtained for the copper substituted complexes (Fig. 8) show a non-linear time dependence both upon illumination and when the excitation source is removed, indicating the presence of persistent photoconductivity (PPC). This behaviour is shown both with excitation at 445 nm and 671 nm and differs from that of NiTMPyP:H_2TSPP and the H_2TMPyP:NiTSPP. It also differs from the H_2TMPyP:H_2TSPP when excited at 671 nm. The H_2TMPyP:H_2TSPP crystals also showed PPC when excited at 445 nm.

The PPC decay for the CuTMPyP:H_2TSPP and H_2TMPyP:CuTSPP crystals can be fitted using the stretched exponential function previously described for the PPC signal of the H_2TMPyP:H_2TSPP system, [30,77]:

$$I(t) = I_{PPC} \exp\left[-\left(\frac{t}{\tau}\right)^{\beta}\right] + I_{NPC}F(t) \qquad (1)$$

where I_{PPC} is the initial current from the persistent photoconductivity; τ is a weighted average lifetime (s); β is a stretching factor; I_{NPC} is the non-persistent photocurrent; and F(t) is a function describing the time dependence associated with I_{NPC}, primarily arising from the time constant of the electronics used to measure the current. While analysing the PPC data, only data obtained four seconds after illumination ended was considered in order to remove any contributions from the non-persistent photoconductivity.

Quantification of PPC decay curves for the copper BP systems acquired with the 445 nm laser irradiation at variable temperatures is depicted in Table 1. The contribution of PPC to the photoresponse of CuTMPyP:H_2TSPP exposed to the 671 nm laser was too small to be reliably extracted. Room temperature excitation of H_2TMPyP:CuTSPP with 671 nm laser yielded τ = 162 s and β = 0.43 while excitation at 445 nm gave τ = 308 s and β = 0.46. When the sample was annealed to 100 °C (Table 1), β remained relatively constant across the temperature range for both excitations wavelengths. The observed lifetimes however, decreased substantially with increasing temperatures indicating a thermally activated conduction process. Plotting ln(τ) vs 1/T

Table 1. Representative values for PPC current, time constant, and β as function of temperature for a H_2TMPyP:CuTSPP and CuTMPyP:H_2TSPP samples under laser irradiation (6 mW 671 nm and 8 mW 445 nm).

T (K)	H_2TMPyP:CuTSPP						CuTMPyP:H_2TSPP		
	671 Laser Illumination			445 nm Laser Illumination			445 nm Laser Illumination		
	I_{PPC} (pA)	τ (s)	β	I_{PPC} (pA)	τ (s)	β	I_{PPC} (pA)	τ (s)	β
298	26	162	0.43	2920	308	0.46	32	1727	0.40
323	69	130	0.40	4550	253	0.46	39	942	0.36
348	214	86	0.44	8190	162	0.44	45	444	0.36
373	769	45	0.40	15230	92	0.42	51	230	0.33

showed that the lifetimes exhibit Arrhenius behaviour, with E_A = 153 meV for 445 nm excitation and E_A = 158 meV for 671 nm excitation (Table 2 and Fig. S15 in the ESI). The similarities of β, τ, and E_A obtained by irradiating H2TMPyP:CuTSPP at 445 nm and 671 nm strongly suggest a similar PPC mechanism for both these excitations.

The CuTMPyP:H_2TSPP complex exhibits very weak persistent photoconductivity when excited with a 445 nm laser line (Fig. 8, Table 1). The lifetime at 25 °C is noticeably large, 1727 s, and deceases when the BP sample is heated to 100 °C with E_A = 260 meV; β is relativity unaffected by the rise in temperature. For comparison, the PPC observed in the zwitterionic TSPP nanorods,[78] fitted to the same function as in equation (2) yielded τ of 1500 s with β = 0.55.

In semiconducting materials where the stretched exponential function has been used to model the decay of the PPC, β has been associated with the dimensionality of the charge transfer processes, where for a one-dimensional charge transport process has β < 0.5.[79,80,81] In the TMPyP:TSPP material[30] and its copper derivatives (Table 2), β is averages approximately 0.40, suggesting a one-dimensional charge transfer process. This is consistent with the hypothesis that conduction in these materials is facilitated via π-π interactions. In the BP crystals we studied, all of the π-π interactions occur along the a-axis, or along the length of the nanorods.

Unlike the H_2TMPyP:H_2TSPP crystals which are nonconducting in the dark,[30] all four metallated ISA conduct weakly in the dark and their conductivity increases with increasing temperature (Table 2, Fig. S15 in the ESI†). The temperature dependence of their conductivity fits using the Arrhenius. The extracted activation energy of the dark conductivity for the metallated ISAs is shown in Table 2. It is possible that this activation energy describes either the energy required to separate electron-hole pairs or the energy required for an electron to be thermally excited over a Schottky barrier.[82]

The values for the room temperature dark conductivity of the metallated ionic porphyrin crystals range between 10^{-11} and 10^{-13} Ω^{-1} m^{-1} while their photoinduced response measure up to five orders of magnitude higher (see Table 2). Among these, H_2TMPyP:CuTSPP exhibited the highest photocurrent with the 445 nm illumination. The conductivity values for the ISA porphyrin series in Table 2 are comparable to the amounts reported for other ionic and neutral porphyrin based solids (the actual structure for most of these materials have not been uniquely determined). Electrical conductivity of a tetragonal single crystal of 5,10,15,20-tetrakis (4-N-ethylpyridyl) porphyrin salt, $[H_2TEPyP^{4+}][4I^-]$ exhibited high anisotropy, in that the dark conductivity along the stacking column (σ||) equalled 3.2 × 10^{-8} Ω^{-1} cm^{-1} and was three orders of magnitude larger than that perpendicular to the stacking column.[83] Anisotropic conductivity is common in organic crystals because charge flow along the π stacking axis is generally more facile than perpendicular (σ⊥) to the chromophore columns. Charge recombination and charge trapping processes were suggested as possible conductance mechanisms. The photoconductivity of Langmuir-Blodgett films composed from chlorophyll–*a* investigated by Jones was also directional with σ⊥ = 1.0x10^{-10} Ω^{-1} m^{-1} while σ|| ≤ 1.0x10^{-8} Ω^{-1} m^{-1}. The dark conductivity for these films averaged 5x10^{-13} Ω^{-1} m^{-1}.[84] A network of filaments comprised of tetra-meso-amidophenyl substituted porphyrin with long alkyl side chains gave rise to σ = 1.4x10^{-9} Ω^{-1}·m^{-1} with

Table 2. Comparison of dark conductivity and photoconductivity (NPC and PPC) activation energies (E_A) for the free-base and metallated ISA porphyrins. Included are room temperature conductance and photo conductance values, σ|| (Ω^{-1} m^{-1}). Laser intensity for the 445 nm and 671 nm excitations was 1.0 W cm^{-2}.

Porphyrin System	E_A for Dark Conductivity (mV)	E_A (671 nm Laser)		E_A (445 nm Laser)		Dark Conductivity (Ω^{-1} m^{-1})	Photoconductivity 445 nm Laser (Ω^{-1} m^{-1})
		NPC (mV)	PPC (mV)	NPC (mV)	PPC (mV)		
H_2TMPyP:H_2TSPP	---	205	---	22	126	---	4.0 x 10^{-8}
H_2TMPyP:CuTSPP	550	144	426	61	210	6.7 x 10^{-11}	7.7 x 10^{-8}
CuTMPyP:H_2TSPP	203	99	---	58	20	3.5 x 10^{-11}	1.1 x 10^{-8}
H_2TMPyP:NiTSPP	764	149	---	80	---	7.7 x 10^{-11}	7.7 x 10^{-9}
NiTMPyP:H_2TSPP	666	101	---	97	---	5.97 x 10^{-12}	6.3 x 10^{-9}

420 nm laser excitation.[85] The direct electrical conductivity of nanoscale networks composed of CoTPyP and SnTPPS ions at 23 °C measured 2x10^{-8} Ω^{-1} cm^{-1} and increased by 20% when the aggregates were exposed to light but declined with sample heating.[86]

Nanorods of zwitterionic H_2[H_2TSPP] studied by Schwab[78,87] and Riley[88] while insulating in the dark displayed a much higher photoconductivity signal of 6.4x10^{-3} Ω^{-1} cm^{-1} (on exposure to 488.0 nm laser) than our binary ionic poprhyryn systems. Friesen et al. investigated electron transport in TSPP aggregates by employing Scanning Tunneling Microscopy (STM) imaging and Orbital Mediated Tunneling Spectroscopy (OMTS).[29,89,90] The TSPP nanorods were found to be rectifying, exhibiting a dramatic increase in conductivity above +1 V bias which was ascribed to a band formed from the combined LUMOs of the porphyrin zwitterions.[89,89] Conductive AFM studies of the SnT(*N*-EtOH-4-Py)P:ZnTSPP porphyrin crystalline nanostructures carried out by Medforth and Shellnut revealed 5-fold increase in current between the substrate and the tip when the porphyrin sample was illuminated with incandescent light.[22] Quantification of photoconductivity was not given.

Low conductance and low photoconductivity in organic semiconductors may be improved by introducing charge acceptors (e.g. I_2, Br_2) into p-type crystals or charge donors (e.g. Na^+, K^+) into n-type materials.[91-94] The conductivity of p-type semiconductor, azodioxy-linked porphyrin-based covalent organic framework (COF), increased by more than three orders of magnitude with iodine doping into its pores (1.9 nm in diameter). Moreover, I_2-doped COF shows significantly enhanced photo-current generation when irradiated with light.[95] Since tetraphenylporphyrin is a p-type photoconductor[95] doping the binary porphyrin series that we have studied with iodine or bromine may improve their photoconductivity. Enhancement in photoresponse was also reported for dye-sensitized solar cells (DSSCs) where halogen-bonding interactions formed between a nucleophilic electrolyte species (I^-) and a photo-oxidized triphenylamine-based dye immobilized on a TiO_2 surface.[96] The crystalline channels in the TMPyP:TSPP class of compounds are ~0.5 nm in width and are large enough to admit halides (neutral or charged), or alkali cations. We are currently performing halogen doping experiments of the BP crystals.

Periodic quantum calculations

To further understand the electronic properties and explain the photoconductive behaviour of the metallated BPs, we performed periodic DFT calculations and EHTB calculations. Crystal structures of H_2TMPyP:(M)TSPP and (M)TMPyP:H_2TSPP, where M= Ni/Cu were created by changing the core substitution of the H_2TMPyP:NiTSPP crystals and then optimizing the structure. As with the calculations based on the H_2TMPyP:H_2TSPP crystal structure,[30] water molecules were omitted because they do not lie between the porphyrin chromophores (Fig. 3) and thus should not interfere with the simulated band structure and electronic conduction along the *a*-axis.

The DFT calculated band structures and corresponding densities of states (DOS) for H_2TMPyP:NiTSPP and NiTMPyP:H_2TSPP are presented in Fig. 9, S16, S17. For the NiTSPP:H_2TMPyP crystals the top of the valence band is populated by the NiTSPP while the bottom of the conduction band is populated by the H_2TMPyP. Just like in the free base BPs,[30] there appears to be little mixing of the H_2TMPyP and NiTSPP states in the vicinity of the fermi level (E_f), Figure 9a. The top of the valence band is populated by doubly occupied Ni d-orbitals (of all kinds). Nickel bands of NiTSPP have little mixing with the TSPP but no mixing with TMPyP π-orbitals and the calculated band gap is 1.0 eV, which is unchanged from freebase BPs.[30] One significant difference between the band structure of

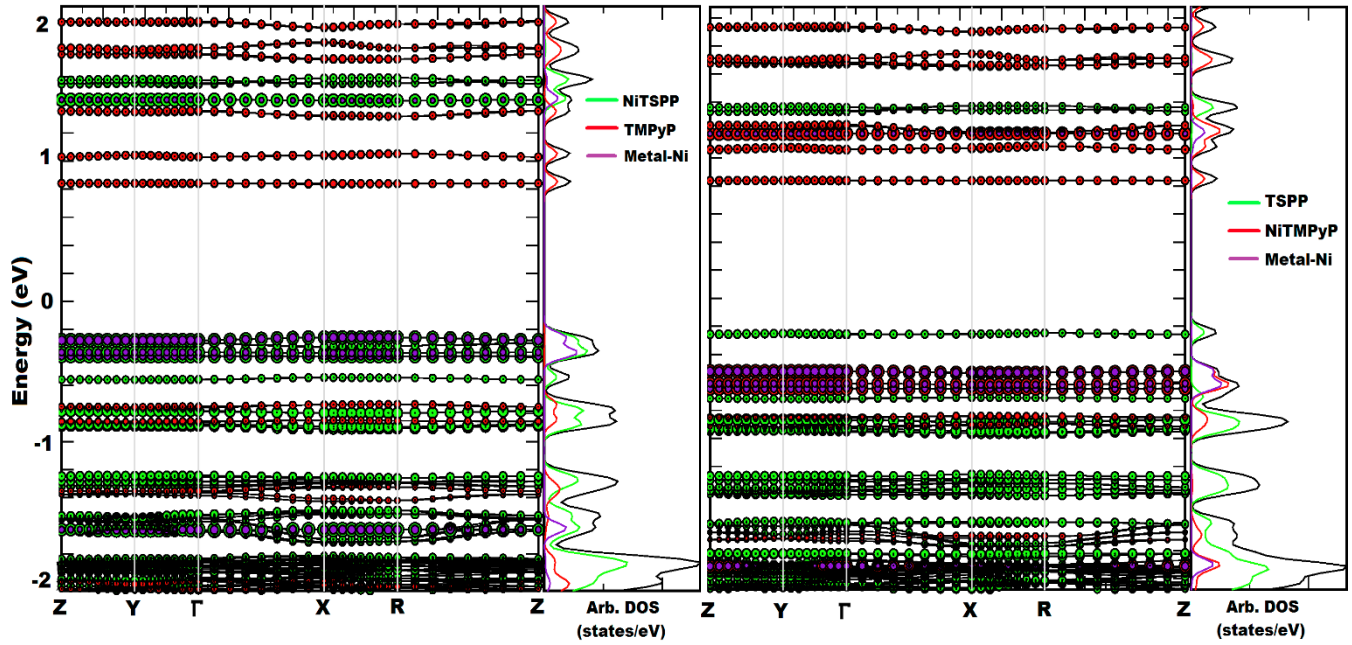

Fig. 9 Projected density of states and band structure for the (a) H_2TMPyP:NiTSPP and (b) NiTMPyP:H_2TSPP crystals computed from DFT. The Fermi level (E_f) is set at zero. The high symmetry points the Brillouin zone are as follows, Γ = (0,0,0), Z = (0,0,0.5), Y = (0,0.5,0), X = (0.5,0,0), R = (0.5,0.5,0.5).

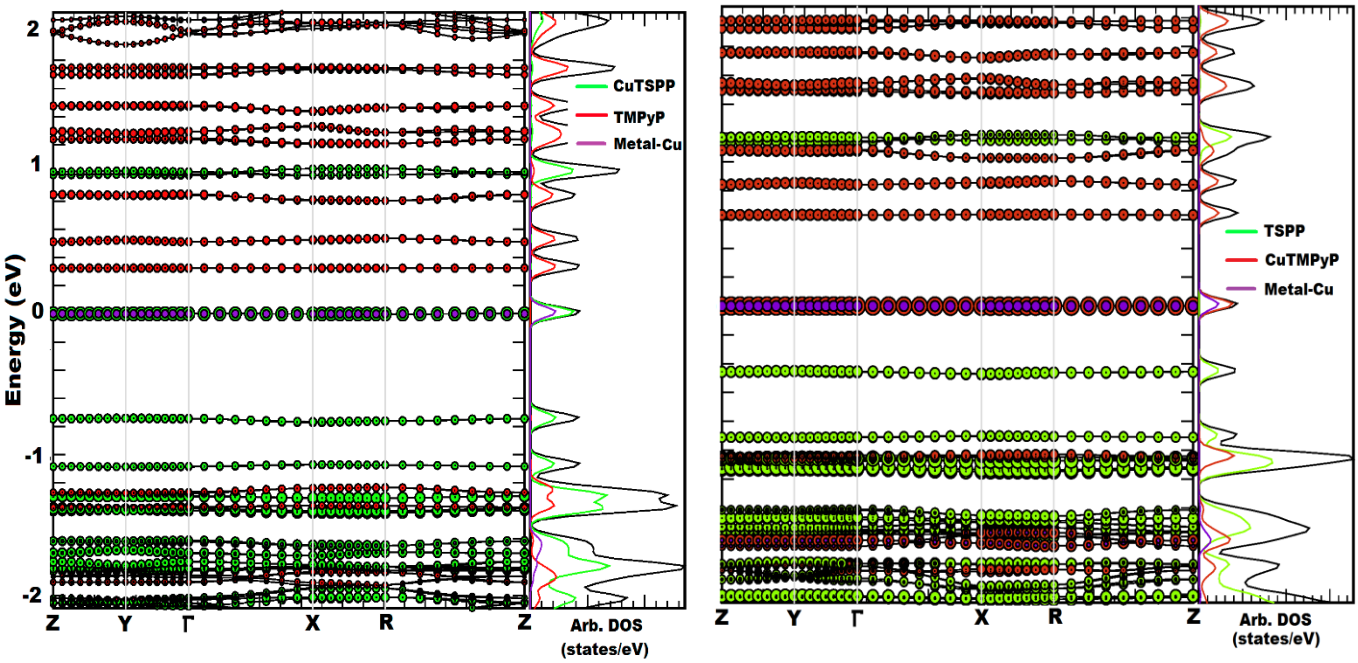

Fig. 10 Projected density of states and band structure for H_2TMPyP:CuTSPP and CuTMPyP: H_2TSPP crystals computed from DFT. The Fermi level (E_f) is set at zero.

metallated and freebase structures is that the valence bands of $-SO_3$ substituents (see near -0.8 eV in Fig. 9a, S16) of NiTSPP align with that of TMPyP contrary to bands in H_2TMPyP:H_2TSPP (Figure 10a and S6 in reference 30). Similar observations were made for NiTMPyP:H_2TSPP crystal (Fig. 9b, S17). In the vicinity of E_f, Ni bands of NiTMPyP has little mixing with π-orbitals of TMPyP but no mixing with TSPP. One significant difference between having Ni on the TMPyP vs. on the TSPP is that the Ni bands are not the frontier bands in NiTMPyP:H_2TSPP crystals. The band gap remains at 1.0 eV.

Band structures for Cu metallated BPs (Fig. 10) are interesting and showed some significant differences from the free base only BPs[30] and with Ni metallated BPs (Fig. 9). The DFT calculated band gap for H_2TMPyP:CuTSPP crystal (Figure 10a, S18) is found be 0.36 eV with a singly occupied Cu band at the top of the valence band. Since the exact position of the fermi level is subject to debate in PW-DFT calculations,[97,98] based on Fig. 10a we can place an upper limit for the band gap to be 0.76 eV. Hence, the band gap for H_2TMPyP:CuTSPP is at least 0.25 eV lower than that observed for free base only BPs[30] and with Ni metallated BPs (Fig. 9). Although there is little mixing between the CuTSPP and TMPyP bands at the vicinity of the band gap, we think the lowered band gap upon adding Cu^{+2} to TSPP led to lower activation energy in H_2TMPyP:CuTSPP rods (Table 2). Similar observations were made if Cu^{+2} is added on TMPyP instead of TSPP. The calculated band gap for CuTMPyP:H_2TSPP system (Figure 10b, S19) is found to be at least 0.65 eV which is consistent with the determined activation energy for CuTMPyP:H_2TSPP crystal (Table 2). This behaviour can be further confirmed by EHTB calculations shown later in the study.

Similar to our previous work[30] on H_2TMPyP:H_2TSPP crystals, we performed EHTB calculations on DFT optimized structures of Ni and Cu BPs. The band structures for Ni and Cu BPs are depicted in figures S20-S23. As noted earlier, DFT tends to underestimate band gaps and we found that to be also true for metallated BPs. For nickel metallated porphyrins the band gaps increased from about 1eV in DFT to ~1.6 eV in EHTB. This is also consistent with what was observed in the free base porphyrins.[30] The band gap for copper BPs has increased from 0.76 eV to ~1.0 eV, which is ~0.6 eV lower than that for freebase and Ni BPs. These band structures match with DFT findings. Furthermore, occupancies of the metal bands calculated with EHTB also match with DFT calculations, i.e.; Ni has doubly occupied while Cu has single occupied frontier bands. EHTB calculations also showed that the effective mass (m*) of a hole at the bottom of the conduction band for the H_2TMPyP:CuTSPP was 120.85 m_e (where m_e = mass of an electron) and the effective mass of an electron at the top of the valence band equalled -10.26 m_e. In H_2TMPyP:CuTSPP the hole and electron effective masses in the frontier orbitals (bottom of conduction and top of valence) are 65.51 m_e and -12.26 m_e respectively. The m* of both Ni BPs are similar to that of H_2TMPyP:CuTSPP. For the H_2TMPyP:NiTSPP, the hole effective mass was 77.46 m_e while the electron effective mass was -10.44 m_e, while in NiTMPyP:H_2TSPP the hole and electron effective masses were 66.64 m_e and -12.37 m_e respectively for frontier orbitals. These are consistent with the field effect experiments that showed that the primary charge carriers for these photoexcited systems were electrons.

Proposed models for photoconductivity (NPC and PPC)

Nonpersistent photoconductivity

The H_2TMPyP:NiTSPP crystalline rods do not exhibit persistent photoconductivity with excitation at 445 nm or at 671 nm, suggesting that all of the conduction through the

crystals is due to band conduction. The photoconductivity is also proportional to the number of photons absorbed. Furthermore, the temperature dependence of the photoconductivity suggests that the mechanism of the optical response is, at least in part, a thermally activated process. This temperature dependence likely arises from the energy required to separate the photogenerated electron-hole pair. The low photoconductivity of the H_2TMPyP:NiTSPP rods relative to the H_2TMPyP:H_2TSPP rods is because the Ni in the NiTSPP causes the charge carrier recombination rate to dramatically increase. Kobayshi *et al.* observed that Ni(II) protoporphyrin exhibited extremely short-lived transient absorption, with the decay back to the ground state having a lifetime of 270 ps.[99] The short lifetime was a result of internal conversion from the lowest energy singlet state of the porphyrin into a low-lying d-d transition singlet state on the Ni.[65,66,100,101,102,103] Others have attributed the lack of fluorescence in Ni(II) porphyrin complexes to this same phenomenon.[104] Therefore, it is likely that the majority of photogenerated charge carriers in the H_2TMPyP:NiTSPP crystals transfer energy to a nickel d-d transition state causing the lifetime of the photocarriers to decrease thereby decreasing the photoconductivity. This could also explain why these rods do not exhibit persistent photoconductivity: the excited states simply do not exist for long enough for photoinduced defects to form. The lack of luminescence from the BPC containing the NiTMPyP or NiTSPP ions supports these obesrvations.

The photoresponsivity of the NiTMPyP:H_2TSPP crystals generally behaves in a similar way to the H_2TMPyP:NiTSPP rods, with either excitation at 445 nm or 671 nm which can be attributed to the internal conversion of excited electrons into a Ni d-d transition state. The lack of correspondence between the action spectrum and UV-vis DRS absorbance of the H_2TMPyP:NiTSPP system is indicative of extremely quenched photoconductivity with excitations in the Soret band. The quenched PC is a result of a low conversion efficiency between the excited states accessed through Soret band excitation and the states responsible for the conductivity. There may be a larger transition probability between the higher excited state accessed through Soret band excitation and the d-d transition state than between the Q band and the d-d transition state or a lower transition probability between the higher excited state and the conducting state.

The action spectra of both H_2TMPyP:CuTSPP and CuTMPyP:H_2TSPP system mirror their absorption spectrum; the power dependence of the photoconductivity for the BPS both at 445 nm and at 671 nm shows a linear dependence. These results suggest that the number of electrons contributing to the photoconductivity is proportional to the number of photons absorbed. The photocurrent observed in the CuTMPyP:H_2TSPP is significantly lower than what was observed in the H_2TMPyP:CuTSPP. Shelnutt and Medforth observed that the conductivity of metallated binary porphyrin systems is dependent on the location of the metal.[22] In those systems, the species in which the Zn^{2+} was located on the anion and the Sn^{4+} was located on the anion were photoconductive. However, when the Zn^{2+} was located on the cation and Sn^{4+} was located on the anion, the species was completely insulating. These differences were attributed to the electron donating behaviour of Zn porphyrins and the electron accepting behaviour of Sn porphyrins. A similar effect could account for the differences between the CuTMPyP:H_2TSPP and the H_2TMPyP:CuTSPP systems.

Persistent photoconductivity

Unlike the nickel BP systems, the H_2TMPyP:CuTSPP composite exhibits persistent photoconductivity with excitations in both the Soret and in the Q-band. Because the activation energies and lifetimes associated with the PPC decay are similar with both excitations the mechanism associated with the PPC is likely the same regardless of excitation wavelength. The CuTMPyP:H_2TSPP system while under 671 nm excitation exhibits a slow time-dependent rise in direct conductivity but no PPC contribution. When the sample is irradiated with a 445 nm laser, both the non-persistent and persistent conductivities are detected.

There are a few likely explanations for the origin of the PPC of the H_2TMPyP:CuTSPP and the CuTMPyP:H_2TSPP crystals. In our previous work on the H_2TMPyP:H_2TSPP rods,[30] we proposed that the source of the PPC was the formation of photo-induced metastable defects (PIDs), which likely arise from changes in the equilibrium geometry of porphyrins within the nanostructure. These changes cause the energy levels of the HOMOs and LUMOs of those molecules to shift, causing mid-gap states near the Fermi level of the Au electrodes to form. The formation of these states allow for a hopping conductivity mechanism. When the excitation source is shut off, these PID states persist for some time, but eventually return to their initial equilibrium geometry. In the H_2TMPyP:H_2TSPP nanorods, persistence was only observed with excitations in the Soret band, suggesting that the activation energy for the formation of the PIDs was quite high. This behaviour is similar to what was observed with the CuTMPyP:H_2TSPP. It is possible that the PPC observed in the H_2TMPyP:CuTSPP and the CuTMPyP:H_2TSPP is due to the same mechanism, but the presence of the Cu in the TSPP lowers the activation energy for the formation of the PIDs, causing the rods to exhibit PPC with excitations in the Q-band as well as excitations in the Soret band. The presence of Cu in the TMPyP does not seem to have as strong of an effect on the activation energy for the formation of the PIDs.

The hopping rate between two photo-induced metastable defects *i* and *j*, ν_{ij}, was discussed previously[30] and can be described as

$$\nu_{ij} = \nu_0 \exp\left(-2\frac{R_{ij}}{b} - \frac{|\varepsilon_j-\varepsilon_i|+(\varepsilon_j-\varepsilon_i)}{2k_BT}\right) \qquad (2)$$

where R_{ij} is the distance between sites *i* and *j* (Å), ν_0 is the hopping attempt frequency (Hz); ε_i and ε_j are the energies of sites *i* and *j* (eV); and *b* is the localization radius of a charge carrier (Å).[105,106] Increasing the number of defects, N, decreases the average distance separating defects, *a*, where $a = N^{-1/3} = \langle R_{ij} \rangle$, resulting in an increase in ν_{ij}. Increasing the hopping rate results in an increase in drift mobility:

$$\mu_e = \frac{ea^2 v_{ij}}{k_B T} \quad (3)$$

where μ_e is the drift mobility and e is the elementary charge. As the samples are illuminated, the PID concentration increases, resulting in an increase in mobility. When illumination ceases, the PID concentration slowly decreases, resulting in the slow decrease in electron mobility over time. Eventually, enough of the defects have relaxed that hopping is no longer possible and the nanorods are once again insulating. In this case, the E_A for the PPC (listed in Table 1) would be the activation energy associated with hopping between sites.

Another potential rationale for the PPC response of the H_2TMPyP:CuTSPP may be associated with the possible presence of adsorbed oxygen. Earlier Schwab and co-workers proposed that the zwitterionic TSPP nanorods behave as insulators in the dark because of surface bound molecular oxygen, effectively forming of a Schottky barrier, which prevents the transfer of electrons from the nanorods to the electrodes.[73] When the TSPP nanorods were excited with a 488 nm light, the O_2 desorbed from the surface, the height of the Schottky barrier decreased and electrons flowed between the rods and the electrodes. When the illumination stopped, O_2 slowly readsorbed to the surface of the nanorods suppressing the electrons transfer. Excess negative charge either as chemisorbed O_2 (in the form of O_2, like the TSPP rods) or surface states acting as electron acceptors, was also thought responsible for the PPC in ZnO nanorods.[107,108] Because the photoconductivity experiments in this study were performed under vacuum (~5 mTorr) where amounts of O_2 are exceedingly low (<1 mTorr partial pressure), it is unlikely that the adsorption/desorption of O_2 is solely responsible for the observed PPC of the H_2TMPyP:CuTSPP crystals.

Conclusions

We synthesized high quality (up to mm long) rodlike crystals of NiTMPyP:H_2TSPP, H_2TMPyP:NiTSPP, CuTMPyP:H_2TSPP, and H_2TMPyP:CuTSPP by applying a previously developed nucleation and growth model.[31] Metal inclusion in one of the ionic porphyrin synthons results in the formation of crystals with nearly identical crystal structures to the free-base analogue H_2TMPyP:H_2TSPP monoclinic system. Dual metal core substitution significantly modifies the crystal geometry. Heating the BP crystals causes significant changes in their crystal structure due to the loss of the water from within the crystalline channels. When samples are annealed to 100 ° C or less they can be rehydrated and exhibit the same XRD patterns as the diffraction data acquired from original unheated samples supporting their extraordinary structural stability. Strong intermolecular electrostatic attractions preserve the integrity of the crystal structures and minimize the potential impairment of their conductive and photoconductive properties when BPs are subjected to thermal treatments. The dehydration/rehydration process is completely reversible suggesting the potential usage of the metallated BPs as gas sensors.

The metallated porphyrin crystalline solids are n-type photoconductors and recombination mechanism of their photogenerated charge follows first order kinetics. They all exhibit dark conductivity (nominal) and direct photoconductivity that are both strongly temperature dependent. The observed direct photoresponse in the Ni^{2+} and Cu^{2+} substituted BPs can be attributed to conventional band conduction. The number of electrons contributing to the photocurrent is directly proportional to the number of photons absorbed thus, the mechanisms of the photoconductivity resulting from excitations within the Soret band and the Q-band are the same.

Both of the Cu^{2+} based BPs exhibit stronger direct photoconductivity than their Ni^{+2} counterparts with the H_2TMPyP:CuTSPP system yielding the highest σ value of the BP series and the H_2TMPyP:TSPP parent system as well. This results is readily explained by DFT band structures calculations which place the band gap for copper based BPs at least 0.25 to 0.35 eV lower than the 1 eV gap observed for the Ni^{2+} analogues and the free-base parent composite.[30] Consistent with the DFT results is the trend in activation energies determined for all of the BPs series studied. The low photoconductivity of the Ni^{2+} based BPs is the result of energy transfer from photogenerated charge carriers the to a nickel d-d transition state causing the lifetime of the photocarriers to decrease thereby decreasing the photoconductivity.

The origin of the PPC in the H_2TMPyP:CuTSPP and the CuTMPyP:H_2TSPP is likely due the formation of photo-induced metastable defects (PIDs), which may arise from changes in the equilibrium geometry of porphyrins within the crystal structure. This same source of the PPC was proposed in the case of H_2TMPyP:H_2TSPP.[30] The presence of Cu^{2+} in the BPs lowers the activation energy for the formation of the PIDs, causing the rods to exhibit PPC with excitations in the Q-band as well as excitations in the Soret band. The PPC decay can be modeled using a stretched exponential function. The value of β (stretching factor) obtained using this fit is consistent with a one-dimensional charge transfer process facilitated by the strong π-π interactions along the stacking direction (*a* crystallographic axis) of the crystal.

In summary, inclusion of a metal in the core of one of the BPs preserves the geometrical structure of the H_2TMPyP:H_2TSPP parent crystal system but modifies its photoresponsivity contingent on the occupation of the metal d-orbitals relative to the band gap of the semiconductor. Thus the photoactivity can be significantly improved by adding Cu^{2+} ion to the porphyrin tecton core or reduced as in the case of Ni^{2+} substitution. Consequently, the molecular organization and intermolecular interactions as well as the electronic states introduced by metal substitution impact the optical and electronic properties of the BP semiconductor. In addition, factors such as the formation of metastable defects and the rates of internal conversion also influence the photoelectronic properties of these materials. Computational modeling can be used to explain and predict the prompt conductive and photoconductive behavior of these materials and provide guidance for optimizing photo response with judicious selection of metal substituents. Predicting and tailoring the persistent photoconductivity will require the identification of the detailed structure of the photo induced defects. Connecting the optoelectronic properties and structure of ionic porphyrin crystals,

and molecular semiconductors in general, is essential for advancing organic optoelectronic technology.

Acknowledgements

We are grateful to the National Science Foundation for their support of this work in the form of grant CHE-1152951. Computational work was performed using the Cascade supercomputer at EMSL (DOE Office of Science User Facility sponsored by the Office of Biological and Environmental Research) located at Pacific Northwest National Laboratory (PNNL) under grant 48783 and the resources from Kamiak HPC provided by Center for Institutional Research Computing (CIRC) at Washington State University. We also thank the X-Ray diffraction group at Bruker AXS Inc. for solving the crystal structure of the H_2TMPyP:NiTSPP solid and the Francheschi Microscopy and Imaging Center at Washington State University for the use of their fluorescence microscope. We also appreciate the assistance of Professor James Brozik in collecting the luminescence data.

References

1 K. M. Coakley and M. D. McGehee, *Chem. Mater.,* 2004, **16**, 4533–4542.

2 J. H. Jou, S. Kumar, A. Agrawal, T.-H. Li, and S. Sahoo, *J. Mater. Chem. C,* 2015, **3***,* 2974-3002.

3 Y. Yamashita. Advances in Organic Crystal Chemistry. Comprehensive Reviews. R. Tamura and M. Miyata eds. Springer, Japan. 2015, pg. 607-625.

4 E. Manna, T. Xiao, J. Shinar and R. Shinar, *Electronics* 2015, **4,** 688-722.

5 Y.C. Chen, M.W. Lee, L.L. Li and K.J. Lin, *Journal of Macromolecular Science*, *Part B: Physics,* 2008, **47**, 955–966.

6 L. Cook, G. Brewer and W.Wong-Ng, *Crystals*, 2017, **7**, 233/1-233/22.

7. Y. C. Chen, C. Y. Hsu , R. Y. Y. Lin, , C. K. Ho and J. T. Lin, *ChemSusChem*., 2013, **6**, 20-35.

8 M. E. Ragoussi, G. de la Torre G and T. Torres,. *Eur. J. Org. Chem.*, 2013, 2832-2840.

9 H. Imahori, T. Umeyama and S. Ito, *Acc. Chem. Res.* 2009, **42**, 1809-1818.

10 M. Jurow, A. E. Schuckman, J. D. Batteas and M. C. Drain,. *Coord. Chem. Rev.* 2010, **254**, 2297-2310.

11 J. A. A. W. Elemans, R. van Hameren, R. J. M Nolte and A. E. Rowan, *Adv. Mater.*, 2006, **18**, 1251-1266.

12 P. Guo, G. Zhao,P. Chen, B. Lei, L. Jiang, L.; H. Zhang,W. Hu and M. Liu, *ACS Nano* 2014, **8,** 3402-3411.

13 F.Dini, E. Martinelli, G. Pomarico, R. Paolesse, D. Monti, D. Filippini A. D'Amico, I. Lundstrom and C. Di Natale, *Nanotechnology* 2009, **20,** 055502/1-055502/8.

14 D. K. Avasthi, A. Kumar, R. Singhal, A. Tripathi and D. S. Misra, *J. Nanosci. Nanotech*. 2010, **10,** 3767-3779.

15 N. R. Armstrong, W. Wang, D. M. Alloway, D. Placencia, E. Ratcliff and M. Brumbach, *Macromol. Rapid Commun,* 2009*,* **30**, 717–731.

16 A. B. Djurisic, A. M. C. Ng, K. Y. Cheung, M. K. Fung and W. K. Chan, *J. Mater. Sci. & Technol.* 2008, **24,** 563-568.

17 C. A. Berven, V. Dobrokhotov, D. N. McIlroy, S. Chava, R. Abdelrahaman, A. Heieren, J. Dick and W. Barredo, W. *IEEE Sens. J.* 2008, **9**, 930–935.

18 A. Krueger, A. *Nachrichten aus der Chemie* 2009*,* **57,** 273-279.

19 S. Mandal, S. K. Nayak, S. K. Mallampalli and A. Patra, *ACS Appl. Mater. Interfaces* 2014, **6**, 130-136.

20 R. C. George, T. Mugadza, S. Khene, G. O. Egharevba and T. P. Nyokong, *Electroanalysis* 2011, **23,** 1699 - 1708.

21 Y. Chen, A. Li, Z. H. Huang, L. N. Wang and F. Kang, *Nanomaterials*, 2016, **6**, 51/1-51/17.

22 Y. Tian, M. C. Beavers,T. Busani, K. E. Martin,J. L. Jacobsen, B. Q. Mercado, B. S. Swartzentruber, F. van Swol, C. J. Medforth and J. A. Shelnutt, *Nanoscale,* 2012, **4**, 1695-1700.

23 H. Imahori, Y. Kashiwagi, T. Hasobe, M. Kimura, T. Hanada, Y. Nishimura, I. Yamazaki, Y. Araki, O. Ito and S. Fukuzumi, *Thin Solid Films,* 2004, **451**, 580-588.

24 Li X, Jiang Y, Xie G, Tai H, Sun P and Zhang B. *Sensors and Actuators B: Chemical* 2013; **176**: 1191-1196.

25 M. Muccini. *Nat. Mater.* 2006, **5**, 605-613.

26 A. Lennartson, A. Roffey and K. Moth-Poulsen K. *Tetrahedron Lett.*, 2015, **56**, 1457-1465.

27 J. R. Eskelsen, Y. Qi, S. Schneider-Pollack, S. Schmitt, K. W. Hipps and U. Mazur, *Nanoscale,* 2014, **6**, 316-327.

28 S. A. Svatek, L. M. A. Perdigão, A. Stannard, M. B. Wieland, D. V. Kondratuk, H. L. Anderson, J. N. O'Shea and P. H. Beton, *Nano Lett.,* 2013, **13**, 3391-3395.

29 U. Mazur, K. W. Hipps, J. R. Eskelsen and M. Adinehnia, in Handbook of Porphyrin Science, ed. K. M. Kadish, K. M. Smith and R. Guilard, 2016, **40**, 69–103.

30 M. Adinehnia, B. Borders, M. Ruf, B. Chilukuri, K. W. Hipps and U. Mazur, *J. Mater. Chem. C,* 2016*,* **4***,* 10223-10239.

31 M. Adinehnia, U. Mazur and K. W. Hipps, *Cryst. Growth and Design*, 2014, **14**, 6599-6606.

32 C. Barnaba, S. C. Humphreys, A. O. Barden, J. P. Jones and J. A. Brozik, *J. Phys. Chem. B*, 2016, **120**, 3038-3047.

33 X. Zhai, D. Alexander, P. Derosa,.and J.C. Garno. *Langmuir* 2017, **33**, 1132−1138.

34 G. Kresse and J. Furthmüller, *Comput. Mater. Sci.*, 1996, **6**, 15-50.

35 G. Kresse and J. Furthmüller, *Phys. Rev. B: Condens. Matter Mater. Phys.*, 1996, **54**, 11169-11186.

36 R. Hoffmann and W.N. Lipscomb, *J. Chem. Phys.*, 1962, **36**, 2179-2189.

37 R. Hoffmann and W.N. Lipscomb, *J. Chem. Phys.*, 1962, **36**, 3489-3493.

38 R. Hoffmann and W.N. Lipscomb, *J. Chem. Phys.*, 1963, **37**, 520-523.

39 R. Hoffman, *J. Chem. Phys.*, 1963, **39**, 1397-1412.

40 M. H. Whangbo and R. Hoffman, *J. Am. Chem. Soc.*, 1978, **100**, 6093-6098.

41 J. P. Perdew, K. Burke and M. Ernzerhof, *Phys. Rev. Lett.*, 1996, **77**, 3865-3868.

42 G. Kresse and D. Joubert, *Phys. Rev. B: Condens. Matter Mater. Phys.*, 1999, **59**, 1758-1775.

43 P. E. Blöchl, *Phys. Rev. B: Condens. Matter Mater. Phys.*, 1994, **50**, 17953-17979.

44 H. J. Monkhorst and J. D. Pack, *Phys. Rev. B: Solid State*, 1976, **1**, 5188-5192.

45 J. Klimeš, D. R. Bowler and A. Michaelides, *Phys. Rev. B: Condens. Matter Mater. Phys.*, 2011, **83**, 195131.

46 K. Lee, É. D. Murray, L. Kong, B. I. Lundqvist and D. C. Langreth, *Phys. Rev. B: Condens. Matter Mater. Phys.*, 2010, **82**, 081101/1-081101/4.

47 J. Klimeš, R. B. David and A. Michaelides, *J. Phys.: Condens. Matter*, 2010, **22**, 022201/1-022201/5.

48 B. Chilukuri, U. Mazur and K. W. Hipps, *Phys. Chem. Chem. Phys.*, 2014, **16**, 14096-14107.

49 M. C. Payne, M. P. Teter, D. C. Allan, T. A. Arias and J. D. Joannopoulos, *Rev. Mod. Phys.*, 192, **64**, 1045-1097.

50 E. N. Brother, A. F. Izmaylov, J. O. Normand, V. Barone and G. E. Scuseria, *J. Chem. Phys.*, 2008, **129,** 011102/1-011102/4.

51 J. Perdew, *Int. J. Quantum Chem.*, 1985, **28**, 497-523.

52 D. Kienle, J. I. Cerdá and A. W. Ghosh, *J. Appl. Phys.,* 2006, **100,** 043715/1-043715/8.

53 E. B. Lopes, H. Alves, E. Ribera, M. Mas-Torrent, P. Auban-Senzier, E. Canadell, R. T. Henriques, M. Almeida, E. Molins, J. Veciana, C. Rovira and D. Jerome, *Eur. Phys. J.,* 2002, **B29**, 27-33.

54 T. R. Cundari, B. Chilukuri, J. M. Hudson, C. Minot, M. A. Omary and H. Rabaâ, Organometallics, 2010, **29**, 795-800.

55 E. B. Lopes, H. Alves, E. Ribera, M. Mas-Torrent, P. Auban-

56 Virtual NanoLab version 2015.1, QuantumWise A/S, Copenhagen, Denmark.

57 C.T. Chantler, *J. Phys. Chem. Ref. Data,* 2000, **29**, 597-1048.

58 D. Prill, P. Juhas, S. J. L. Billinge and M. U. Schmidt, *Acta Cryst.*, 2016, **A72**, 62-72.

59 B. Borders, M. Adinehnia, N. Rosenkranz, M. van Zijll, K. W. Hipps and U.Mazur. *J. Porph. Phthal.,* 2017, **21**, 569–580.

60 F. J. Vergeldt, R. B. M. Koehorst, A. van Hoek and T. J. Schaafsma, *J. Phys. Chem.*, 1995, **99**, 4397–4405.

61 J. V. Hollingsworth, A. J. Richard, M. G. H. Vicente and P. S. Russo, Biomacromolecules, 2012, **13**, 60–72.

62 Z. Wang, C. J. Medforth and J. A. Shelnutt, *J. Am. Chem., Soc.,* 2004, **126**, 15954–15955.

63 A. Antipas, D. Dolphin, M. Gouterman and E. C. Johnson. *J. Am. Chem. Soc.,* 1978, **100**, 7706-7709.

64 A. Harriman, *J.C.S. Faraday I*, 1980, **76**, 1978-1985.

65 R. L. Ake and M. Gouterman, *Theor. Chim. Acta*, 1970, **17**, 408-4016.

66 A. Adamczyk and F. Wilkinson, *J.C.S. Faraday II*, 1972, **68**, 2031-2041.

67 V. S. Chirvonyi, B. M. Dzhabarov, Y. V. Timinskii and G. P. Gurinovich, *Chem. Phys. Lett.*, 1980, **70**, 79-83.

68 D. Kim, C. Kiramair and D. Holten, *Chem. Phys.*, 1983, **75**, 305-322.

69 E. W. Findsen, J. A. Shelnutt and M. R. Ondrias, *J. Phys. Chem.*, 1988, **92**, 307-314.

70 A. Y. Chikisev, V. F. Kamalov, N. I. Korteev, V. V. Kvach, A. P. Shkvrinov and B. N. Toleutaev, *Chem. Phys. Lett.*, 1988, **144**, 90-95.

71 M. Natali and F. Scandola. *J. Phys. Chem. A.*, 2016, **120**, 1588-1600.

72 S. Srisonphan, S. J. Juan and H. K. Kim, *Nat. Nanotechnol.*, 2012, **7**, 504-508.

73 C. K. Riley, E. A. Muller, B. E. Feldman, C. M. Cross, K. L. Van Aken, D. E. Johnston, Y. Lu, A. T. Johnson, J. C. de Paula and W. F. Smith, *J. Phys. Chem. C*, 2010, **114**, 19227-19233.

74 F. Yakuphanoglu and B. Filiz Senkal, *Polym. Adv. Technol.,* 2008, **19,** 1193-1198.

75 S.R. Cowan, A. Roy, and A. J. Heeger, *Phys. Rev. B*, 2010**, 82,** 245207/1-245207/10.

76 *Molecular Crystals*. J. D. Wright, ed. Cambridge University Press, Cambridge, U.K. 1995, pg. 184.

77 M. Cardona, R. V. Chamberlin and W. Marx, *Ann. Phys.*, 2007, **16**, 842-845.

78 A. D. Schwab, D. Smith, B. Bond-Watts, D. Johnston, J. Hone, A. Johnson, J. de Paula, J. and W. F. Smith, *Nano Letters,* 2004, **4**, 1261-1265.

79 Y. S. Cohen, S. Xiao, M. L. Steigerwald, C. Nuckolls and C. R. Kagan, *Nano Lett.,* 2006, **6**, 2838–2841.

80 E. Muller-Horsche and D. Haarer, *Phys. Rev. B: Condens. Matter Mater. Phys.*, 1987, **35,** 1273–1280.

81 N. Boden, J. Bushby, J. Clements, K. Donovan, B. Movagharand T. Kreouzis, Phys. Rev. B: Condens. *Matter Mater. Phys.,* 1998, **58,** 3063–3074.

[82] K. Kajijama, Y. Mizushima and S. Sakata, *Appl. Phys. Lett.*, 1973, **23**, 458-459

83 Y. C. Chen, M. W. Lee, L. L. Li and K. J. Lin, *Journal of Macromolecular Science, Part B Physics* 2008, **47**, 955-966.

84 R. Jones, R.H. Tredgold and P. Hodge. *Thin Solid Films*, 1983, **99**, 24-32.

85 A. P. Schall, P. Iavicoli, Z. J Qi, J. Menko, Y. lu, M. Linares, J. C. de Paula, D. B. Amabilino, A. T. Jonson, and W. F. Smith, *J. Phys. Chem. C.,* 2015, **119,** 26154-26163.

86 E. A. Koposova, A. A. Pendin, Y .E. Ermolenko, G. I. Shumilova, A. A. Starikova and Y. G. Mourzina, *Rev. Adv. Mater. Sci.,* 2016, **45**, 15-19.

87 A. L. Yeats, A. D. Schwab, B. Massare, D. E. Johnston, A. T. Johnson, J. C. de Paula and W. F. Smith, *J. Phys. Chem. C,* 2008, **112**, 2170-2176.

88 C. K. Riley, E. A. Muller, B. E. Feldman, C. M. Cross, K. L. Van Aken, D. E. Johnston, Y. Lu, A. T. Johnson, J. C. de Paula and W. F. Smith, *J. Phys. Chem. C,* 2010, **114**, 19227-19233.

89 B. A. Friesen, B. Wiggins, J. L. McHale, U. Mazur and K. W. Hipps, *J. Am. Chem. Soc.,* 2010, **132**, 8554-8556.

90 B. A. Friesen, B. Wiggins, J. L. McHale, U. Mazur and K. W. Hipps, *J. Phys. Chem. C.*, 2011, **115**, 3990-3999.

91 Q. Meng, C. Zhang, Y. Zhang, Y. Zhang, Y. Liao and Z. Dong, *Appl. Phys. Lett.,* 2015, **107**, 043103-043108.

92 F. P Xavier and G. J. Goldsmith. *Bull. Mater, Sci.* 1995, **18**, 283-287.

93 B. Nath, W. H. Li, Ji. H. Huang, G. E. Wang, Z. Hua Fu, M. S. Yao and G. Xu. *CrystEngComm.*, 2016, **18**, 4259-4263.

94 L. M. Cowen, J. Atoyo, M. J. Carnie, D. Baran, and B. C. Schroedera., *ECS J. Solid State Sci. and Tech.,* 2017, **6**, N3080-N3088.

95 M. V. Martinez-Diaz, G. de la Torre and T. Torres, *Chem.Commun.,* 2010, **46**, 7090-7108.

96 S. J. C. Simon, F. G. L. Parlane, W. B. Swords, C. W. Kellett, C. Du, B. Lam, R. K. Dean, K. Hu, G. J. Meyer and C. P. Berlinguette. *J. Am. Chem. Soc.*, 2016, **138**, 10406−10409.

97 G. Kresse and J. Furthmiiller. *Comp. Mat. Sci.*, 1996, **6**, 15-50.

98 N. D. Mermin, Phys. Rev. **137**, A1441.

99 T. Kobayashi, K. D. Straub and P. M. Rentzepis, *Photochem. Photobiol.*, 1979, **29**, 925.

100 V. S. Chirvonyi, B. M. Dzhabarov, Y. V. Timinskii and G. P. Gurinovich, *Chem. Phys. Lett.*, 1980, **70**, 79-83.

101 D. Kim, C. Kiramair and D. Holten, *Chem. Phys.*, 1983, **75**, 305-322.

102 E. W. Findsen, J. A. Shelnutt and M. R. Ondrias, *J. Phys. Chem.*, 1988, **92**, 307-314.

103 A. Y. Chikisev, V. F. Kamalov, N. I. Korteev, V. V. Kvach, A. P. Shkvrinov and B. N. Toleutaev, *Chem. Phys. Lett.*, 1988, **144**, 90-95.

104 A. Harriman, *J.C.S. Faraday I*, 1980, **76**, 1978-1985.

105 D. Monroe, *Phys. Rev. Lett.*, 1984, **54**, 143-149.

106 I. I. Fishchuk, V. I. Arkhipov, A. Kadashchuk, P. Heremans and H. Bässler, *Phys. Rev. B: Condens. Matter Mater. Phys.*, 2007, **76**, 1-12.

107 J. C. Moore and C. v. Thompson, *Sensors*, 2013, **13**, 9921-9940.

108 D. Cammi and C. Ronning, *Adv. Cond. Matt. Phys.*, 2014, **2014**, 1-5.

Experimental and computational structure-function study of an organic crystalline photoconductor composed of metal substituted oppositely charged ionic porphyrins.